International Journal of Refractory Metals and Hard Materials 140 (2026) 107907

Contents lists available at ScienceDirect

International Journal of Refractory Metals and Hard Materials

journal homepage: www.elsevier.com/locate/IJRMHM

Short communication

Distinct orientation dependence of plasticity initiation and subsequent deformation in nanoindented tungsten

Florian Tropper [a,b], Takahito Ohmura [a,b,*]

[a] Research Center for Structural Materials, National Institute for Materials Science (NIMS), 1-2-1 Sengen, Tsukuba 305-0047, Japan
[b] Department of Materials Science and Engineering, Graduate School of Engineering, Kyushu University, 774 Motooka, Nishi-ku, Fukuoka 819-0395, Japan

ARTICLE INFO

Keywords:
Nanoindentation
Tungsten
Orientation-dependence
Yield phenomena
Plastic deformation

ABSTRACT

As refractory metals are increasingly subjected to extreme service conditions, a comprehensive understanding of their fundamental deformation mechanisms has become indispensable, particularly considering the persistent discrepancies between predicted and experimentally observed behavior under complex stress fields. Therefore, nanoindentation on the principal crystallographic planes of pure tungsten single-crystals was performed and revealed a strong influence of crystal orientation on indent appearance, hardness and incipient plasticity. For the (100) surface we observe a confined plastic zone with pronounced pile-up and highest hardness of 5.18 ± 0.07 GPa among the three orientations. Unusually long streaks of dislocations form on the surface of (110)-oriented samples demonstrating tungsten's non-Schmid behavior. The (111) surface exhibits hitherto unreported appearance of slip and highest pop-in loads.

1. Introduction

In the past decades tungsten has become a leading candidate as barrier material in extreme environments. Plasma-facing components in nuclear fusion reactors face neutron bombardment for example. Nanoindentation has been widely used to study these irradiation effects [1–12].

Complex stress fields in indentation deformation give rise to influence of stress components other than those on principal slip systems. Particularly in body-centered cubic (BCC) structures non-Schmid behavior is considered a key factor in plastic behavior and can significantly influence the mechanical material response [13]. While prior nanoindentation work has addressed crystallographic orientations [2,10–12,14,15], key aspects such as residual indent morphology are often missing or insufficiently resolved. Experimental observations remain sparse compared to extensive simulations elucidating underlying mechanisms of incipient plasticity via molecular dynamics and discrete dislocation dynamics simulations [16–23]. This gap is particularly relevant for tungsten, whose non-Schmid behavior challenges the predictive capability of current models.

An early microindentation study examined the (100), (110), (111) surfaces of tungsten and reported highest hardness and pile-up on (100) [24]. Likewise, Zayachuk et al. found higher pile-up in (100)-oriented grains than in (111) with orientation-independent hardness for large nanoindents [25]. Regarding smaller tip radii, Yao et al. reported highest stress for pop-in on (100) but contrarily no differences in hardness [2]. Beake et al. also found higher plasticity initiation stress for (100) than for (111) while measuring higher hardness on (111) and attributed these observations to a higher surface roughness and dislocation density in their (111) sample [14]. The last two studies showed surface roughness on the order of a few nm and did not report indent appearance. Surface observations revealed strong orientation dependence of pile-up morphology [15]. In the past years, studies mostly focused on irradiation effects or high-temperature testing using large indenters with tip radii of several μm [26–28]. Das et al. performed a series of experiments with focus on irradiation effects [10–12] and reported little orientation dependence on indent morphology in unirradiated samples [10].

Here, we present a systematic study of the three primary orientations of tungsten. Using Berkovich nanoindentation, for its common use in hardness testing, complemented by high-resolution topography mapping and electron channeling contrast imaging (ECCI), we directly correlate mechanical response with underlying deformation mechanisms. We reveal orientation-specific effects that are not captured by

* Corresponding author at: Department of Materials Science and Engineering, Graduate School of Engineering, Kyushu University, 774 Motooka, Nishi-ku, Fukuoka 819-0395, Japan.
E-mail address: ohmura.takahito@nims.go.jp (T. Ohmura).

https://doi.org/10.1016/j.ijrmhm.2026.107907
Received 20 April 2026; Received in revised form 28 May 2026; Accepted 6 June 2026
Available online 14 June 2026
0263-4368/© 2026 The Authors. Published by Elsevier Ltd. This is an open access article under the CC BY-NC license (http://creativecommons.org/licenses/by-nc/4.0/).

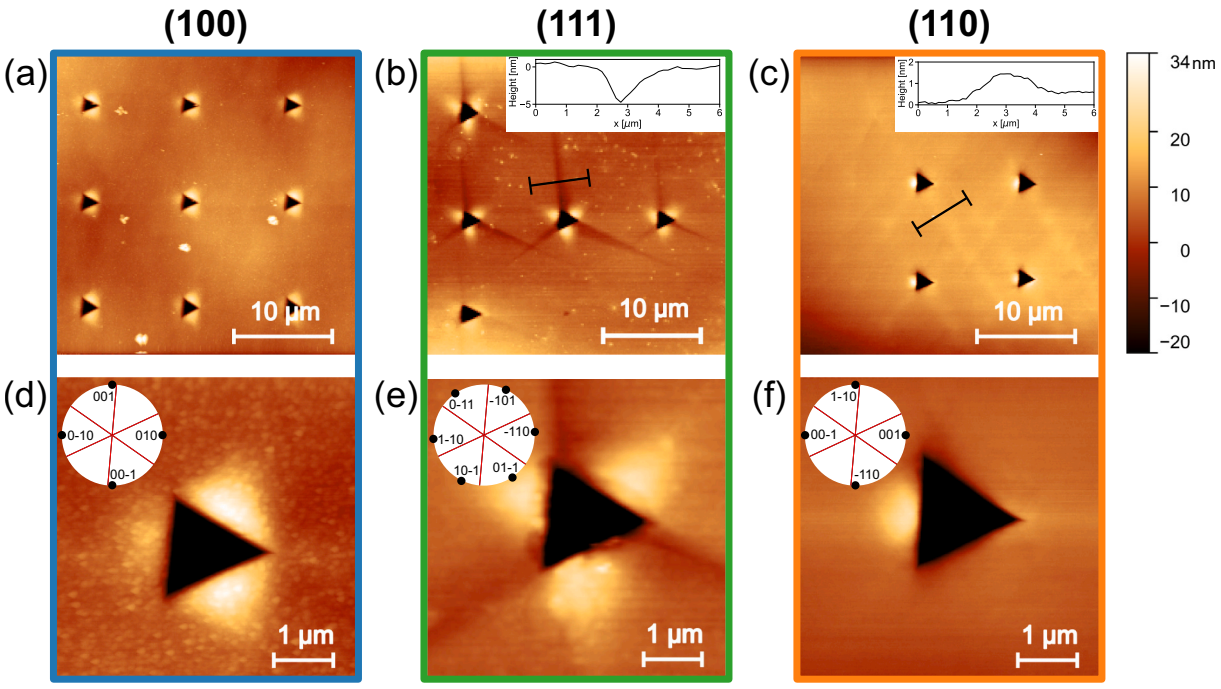


Fig. 1. Surface scans. (a)-(c) Indent maps on the tungsten crystal surfaces (100), (111) and (110). The insets in (b) and (c) show the height profiles along the respective black lines. Images (d)-(f) show the respective magnified scans of single indents. The stereographic projections in the top-left corners show the three sides of an indent (red lines) relative to the indicated poles. (For interpretation of the references to colour in this figure legend, the reader is referred to the web version of this article.)

existing simulations.

2. Materials and methods

The samples studied were three tungsten single crystals with surfaces (100), (110) and (111) and a purity of >99.999 wt% provided by Furuuchi Chemical Corporation (Japan). Each crystal was grown independently via the floating zone method along its respective crystallographic orientation. The manufacturer cut the single-crystals mechanically into discs of 10 mm diameter and 5 mm thickness. The as-received tungsten discs were subsequently prepared by the authors. Without further annealing, mechanical grinding was done using SiC abrasive papers down to grit size of 8 µm followed by polishing with diamond suspensions down to 1 µm particle size. Finally, samples were

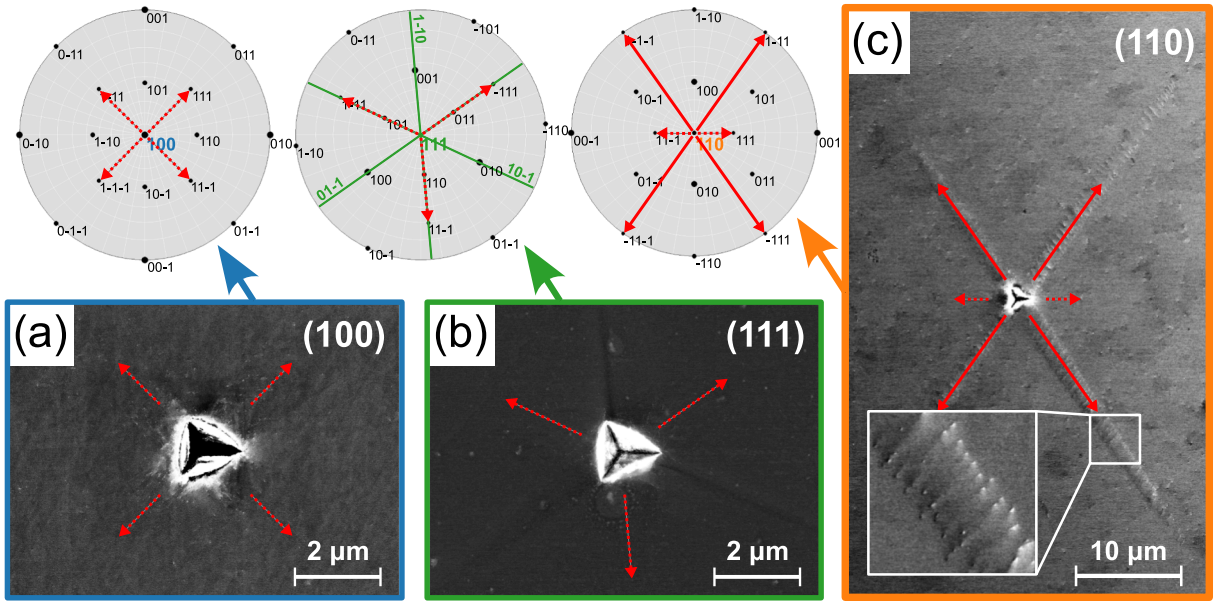


Fig. 2. Electron channeling contrast images. Indents on tungsten surfaces (a) (100), (b) (111) and (c) (110). The latter is exposing long dislocation streaks in ⟨111⟩ directions with Schmid factor zero. The enlarged area shows part of a dislocation streak. (a)-(c) correspond to (d)-(f) in Fig. 1. The red arrows point in the ⟨111⟩ directions of slip. Solid arrows are parallel to the surface (Schmid factor zero) while dotted arrows include an angle with the surface. Stereographic projections of each orientation are provided. Green lines are traces of {110} planes coinciding with groove orientation on the (111) surface. (For interpretation of the references to colour in this figure legend, the reader is referred to the web version of this article.)

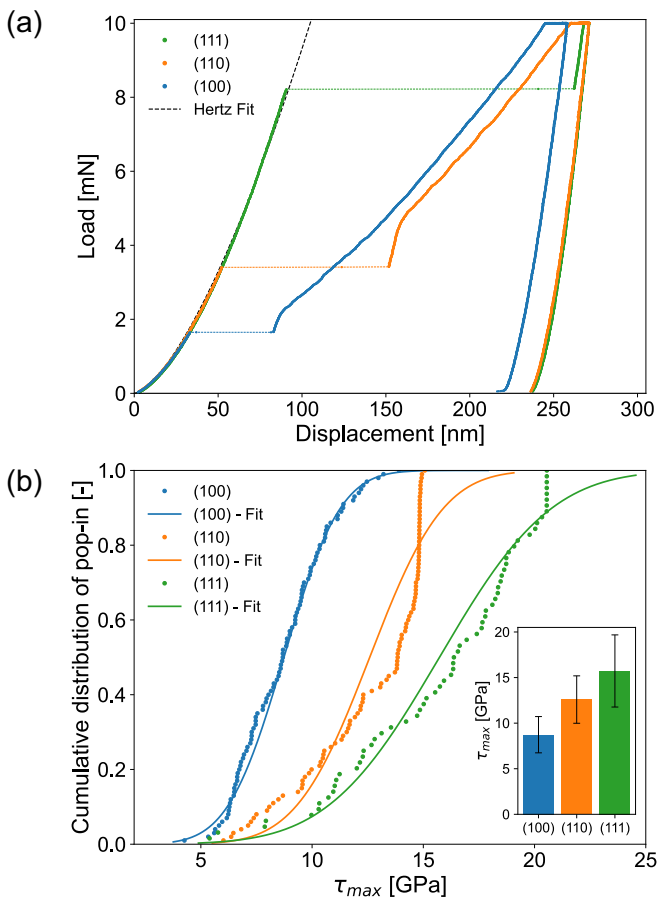


Fig. 3. Nanoindentation results. (a) Representative load displacement curves for the tungsten crystal surface orientations (100), (110) and (111). The elastic part was fitted with an elastic Hertz contact. (b) Cumulative distribution of maximum shear stresses at pop-in τ_{max} for the respective orientations. Each data point corresponds to a first pop-in event and solid lines are fits of Gaussian distributions to the data points. The inset shows the average values of τ_{max} with error bars indicating standard deviations. Note that for the (111) sample only pop-ins that occurred within the tested load regime could be considered.

electropolished using an ice-cold aqueous solution of 2 wt% NaOH to yield surfaces with root mean square roughness of well below 1 nm as determined by 10 × 10 μm surface scans.

One hundred nanoindents were performed per sample on a TI950 TriboIndenter (Bruker, USA) with a loading rate of 1 mN/s up to a peak load of 10 mN using a well-worn diamond Berkovich tip. For all indents the elastic contact could be approximated by the Hertz theory for a spherical contact at the initial stages of the loading curve, therefore an effective tip radius was estimated from the Hertzian model [29] to be approximately 700 nm. It is important to note that this value is model-dependent; while the Hertzian fit strongly supports a spherical-contact approximation during the initial elastic loading regime, it does not definitively confirm that only the spherical portion of the indenter was in contact. To validate this effective radius, independent calibration was performed on a pure iron reference sample, which agrees with the 700 nm estimate (Supplementary Material section I). Moreover, a 5% error of estimated radius only manifests as a 3% deviation in computed shear stresses – insignificant for present qualitative comparison between samples. Indenter tip area function and instrument compliance were carefully calibrated with six indentations performed in dynamic constant stiffness mode on a fused silica reference sample with contact depths ranging from 20 nm to 180 nm following the Oliver–Pharr method. Hardness was assessed at contact depth from the peak load and the corresponding area determined from a standard polynomial area function for the Berkovich geometry (see Supplementary Material section II). Above 80 nm contact depth the computed hardness values remained constant indicating the validity of the area function for deeper penetration depth. Indents were observed in the scanning mode of the TI950 TriboIndenter.

Electron backscatter diffraction (EBSD) was used to determine the crystal orientations in an electron microscope Crossbeam 550 (ZEISS, Germany) equipped with an e-FlashHD electron backscatter detector (Bruker Nano GmbH, Germany) using a step size of 110 nm, an acceleration voltage of 20 kV and a beam current of 10 nA. The same voltage and current were used for ECCI under a working distance of 5.5 mm.

3. Results and discussion

Indentation resulted in differences in mechanical response and particularly in residual imprint appearance. Fig. 1 shows the scanning probe microscopy images of the three tested orientations.

While indents on (100) in Fig. 1(a) and (d) show a confined plastic zone, (111) surfaces show grooves of up to 5 nm depths and radiating out from the indent enclosing exact 120° angles (Fig. 1(b) and (e)). (110)-oriented samples exhibit long X-shaped streaks that rise 1–2 nm above the surface (Fig. 1(c)). ECCI images in Fig. 2 reveal dislocations from up to ~100 nm below the surface [30]. While dislocations are visible close to the indents for (100) and (111)-oriented samples in Fig. 2 (a) and (b), the streaks of the (110) crystal in Fig. 2(c) extend more than ten times the imprint size from the indent. Characteristic dark and bright contrast of dots seen in the inset of Fig. 2(c) indicate end-on dislocations of opposite dislocation line vector and thus dislocation dipoles. The fading contrast between the dipoles and perpendicular to the streaks could mean that the streaks are formed by dislocation half-loops. In that case, the line orientation perpendicular to the direction of propagation would agree with the appearance of punched out half-loops of prismatic dislocations [15,31]. We will link these features with crystallographic considerations and results from mechanical testing.

Table I compares data from nanoindentation for the three crystal orientations. Samples having (111) and (110) surface orientation show very close hardness and depth values whereas indenting on the (100) surface resulted in the highest hardness and smallest depth. Selected load displacement curves from nanoindentation that show values closest to the average values are presented in Fig. 3(a).

We did not observe any noticeable difference in pre-existing dislocation density and the surface roughness was carefully controlled to appear almost identical for all three crystals. Moreover, the data suggest that indentation size effects alone are unlikely to explain the full

Table 1
Comparison of data from nanoindentation and EBSD for the three crystal orientations with surfaces close to (100), (111) and (110). Values are presented as mean ± standard deviation. Euler angles are given in the Bunge convention.

		(100)	(111)	(110)
Hardness [GPa]		5.18 ± 0.07	4.53 ± 0.42	4.66 ± 0.06
Contact depth [nm]		238 ± 2	258 ± 15	253 ± 2
Maximum depth [nm]		258 ± 2	274 ± 14	270 ± 2
Max. Schmid factor for slip system (for uniaxial compression)	{110} ⟨111⟩	0.408	0.272	0.408
	{112} ⟨111⟩	0.471	0.314	0.471
Euler angles of crystal with respect to sample (φ_1; ϕ; φ_2)		225°; 2°; 138°	359°; 44°; 0°	128°; 53°; 226°

hardness difference, while some contribution from depth dependence cannot be excluded (see Supplementary Material section II). Accordingly, the difference may arise from the inherent deformation characteristics of each orientation.

In the following, our results indicate that stress components perpendicular to the slip plane play a major role. As these are also not captured by considering an indentation Schmid factor, we judge that it is sufficient to treat the Schmid factor as a reference and assume uniaxial conditions.

The maximum Schmid factor has same magnitude for common BCC slip systems for the (100) and (110)-oriented samples and is in any case higher than that of (111) (see Table 1). Therefore, the former two are expected to be oriented in softer directions. However, as the opposite is observed, the reason likely lies in how dislocations nucleate and propagate. Slip in tungsten generally takes place on {110} and {112} planes in ⟨111⟩ directions at ambient temperature. Assuming uniaxial compression in the direction of loading, the (100) orientation has four equivalent directions in which dislocations with ⟨111⟩ Burgers vector can be activated (dotted red arrows in Fig.2(a)), while orientations (111) and (110) only have three and two, respectively (dotted red arrows in Fig.2(b) and (c)). If dislocations are nucleated in all four directions, they might interact and impede each other's mobility and therefore increase resistance to deformation and thus hardness. Dislocations around the indent on the (100) face appear to be of mixed character without a preferred slip mode, resulting in a confined plastic zone, consistent with this interpretation.

In all samples plasticity starts with pronounced pop-in, detected here as displacement burst of at least 1 nm. On the (111) surface, pop-in occurred in 63 indentations; the remaining 37 indentations exhibited purely elastic deformation and were systematically excluded from all reported statistics. The other two samples showed pop-in at all indentations.

Fig. 3(b) shows the cumulative distributions of the corresponding maximum shear stresses τ_{max} at pop-in (calculated as in [29]). They appear in a reverse trend compared to hardness (inset in Fig. 3(b)), suggesting that the factors governing hardness and pop-in are fundamentally different. Pop-in for (100) and (111) orientations agree with the expected Gaussian distributions. In the (100) case, the mentioned availability of four ⟨111⟩ directions coupled with relatively high Schmid factors may provide an increased likelihood for a weak spot to be susceptibly oriented within the stressed volume to allow incipient plasticity. Consequently, as plasticity initiation is determined probabilistically, this could explain the lowest average stresses on the (100) surface.

In the (111)-oriented crystal, firstly, resolved shear stresses are expected to only act in three ⟨111⟩ directions with maximum Schmid factor (Fig. 2(b)). Secondly, for these the Schmid factor is lower compared to those of the other crystal orientations (Table 1). Because of these two reasons, the probability of reaching high stress presumably increases, which may result in higher required loads to induce sufficient stress locally for pop-in. Loading on the (110) surface can only activate two Burgers vectors with nonzero Schmid factor. This is statistically disadvantageous for incipient plasticity, thus the probability of reaching high stress is expected to increase with respect to (100). Interestingly, the upper half of the distribution deviates significantly from a Gaussian distribution as pop-ins occur within a tight range of stresses. This points to a transition of incipient plasticity from heterogeneous dislocation nucleation in the bulk to a different competing mechanism that is activated when the stress condition reaches a certain threshold. This mechanism could be linked to a punching out of dislocation half-loops, of potentially prismatic character, that move parallel to the surface, in directions with Schmid factor zero (solid red arrows in Fig. 2(c)), resulting in the observed long streaks. Schmid's law alone cannot account for causing the stresses perpendicular to the compression axis, suggesting a contribution from non-Schmid stress components.

Regarding the (111) surface, the two indents with the smallest displacement burst and lowest pop-in load also lacked detectable grooves (bottom left indent in Fig. 1(b)). Therefore, a certain stress threshold at pop-in is apparently required for their formation. The grooves are aligned with traces of intercepting {110} planes as marked with green lines in the stereographic projection in Fig. 2. No other traces align with the observed groove orientations. Accordingly, the grooves are expected to be the result of pronounced slip. Interestingly with ECCI, no clear dislocation contrast was observed in the grooves up to a tilt of 50° from the backscatter detector (Fig. 2(b)). EBSD with a lateral resolution of about 100 nm [32] revealed no change in orientation along the groove, in agreement with slip. To the authors' knowledge, such pronounced slip lines in nanoindentation have not been reported before. Nanoindentation on BCC (111) faces is uncommon for small-scale methods like nanoindentation as they do not form stable surfaces, like face-centered cubic metals, but instead nanoscopic terraces. This might be the reason why this effect has previously been overlooked.

4. Conclusions

Nanoindentation on the principal crystallographic planes of pure tungsten single-crystals revealed a strong influence of crystal orientation on material response. Incipient plasticity on the (100) surface occurred at lowest loads which might be related to the high number of potentially activated slip systems. On the surface of the (110)-oriented crystal, emission of dislocation streaks was observed for all pop-in events, suggesting the influence of non-Schmid behavior. The number of effective slip systems is only half that of (100), which might account for the increase in pop-in load. Finally, statistically highest resistance to incipient plasticity was observed for the (111) surface orientation, where the presence of three slip systems with only low Schmid factors could be responsible. Pronounced slip during pop-in manifests as grooves on the surface. These findings clearly demonstrate that plasticity initiation at the small scale is highly sensitive to crystallographic orientation.

CRediT authorship contribution statement

Florian Tropper: Writing – review & editing, Writing – original draft, Visualization, Validation, Project administration, Methodology, Investigation, Formal analysis, Data curation, Conceptualization. **Takahito Ohmura:** Writing – review & editing, Supervision, Resources, Project administration, Methodology, Funding acquisition, Conceptualization.

Funding

This work was partially supported by KAKENHI Grants-in-Aid [grant number 24H00389] from the Japan Society for the Promotion of Science (JSPS).

Declaration of competing interest

The authors declare that they have no known competing financial interests or personal relationships that could have appeared to influence the work reported in this paper.

Appendix A. Supplementary data

Supplementary data to this article can be found online at https://doi.org/10.1016/j.ijrmhm.2026.107907.

Data availability

The authors do not have permission to share data.

References

[1] H. Ma, P. Fan, Q. Qian, Q. Zhang, K. Li, S. Zhu, D. Yuan, Nanoindentation test of ion-irradiated materials: issues, Modeling and challenges, Materials 17 (2024), https://doi.org/10.3390/ma17133286.

[2] W.Z. Yao, P. Wang, A. Manhard, C.E. Krill, J.H. You, Effect of hydrogen on the slip resistance of tungsten single crystals, Mater. Sci. Eng. A 559 (2013) 467–473, https://doi.org/10.1016/j.msea.2012.08.127.

[3] J.S.K.L. Gibson, S.G. Roberts, D.E.J. Armstrong, High temperature indentation of helium-implanted tungsten, Mater. Sci. Eng. A 625 (2015) 380–384, https://doi.org/10.1016/j.msea.2014.12.034.

[4] I. Uytdenhouwen, T. Schwarz-Selinger, J.W. Coenen, M. Wirtz, Mechanical and Microstructural Changes in Tungsten Due to Irradiation Damage, Phys. Scr., Institute of Physics Publishing, 2016, https://doi.org/10.1088/0031-8949/T167/1/014007.

[5] D. Terentyev, A. Bakaeva, T. Pardoen, A. Favache, E.E. Zhurkin, Surface hardening induced by high flux plasma in tungsten revealed by nano-indentation, J. Nucl. Mater. 476 (2016) 1–4, https://doi.org/10.1016/j.jnucmat.2016.04.007.

[6] E. Hasenhuetl, R. Kasada, Z. Zhang, K. Yabuuchi, A. Kimura, Ion-irradiation effect on strain rate sensitivity of nanoindentation hardness of W single crystal, Mater. Trans. 58 (2017) 580–586, https://doi.org/10.2320/matertrans.ML201603.

[7] E. Hasenhuetl, R. Kasada, Z. Zhang, K. Yabuuchi, Y.J. Huang, A. Kimura, Evaluation of ion-irradiation hardening of tungsten single crystals by nanoindentation technique considering material pile-up effect, Mater. Trans. 58 (2017) 749–756, https://doi.org/10.2320/matertrans.M2016437.

[8] S. Pathak, S.R. Kalidindi, J.S. Weaver, Y. Wang, R.P. Doerner, N.A. Mara, Probing nanoscale damage gradients in ion-irradiated metals using spherical nanoindentation, Sci. Rep. 7 (2017), https://doi.org/10.1038/s41598-017-12071-6.

[9] O. El-Atwani, J.S. Weaver, E. Esquivel, M. Efe, M.R. Chancey, Y.Q. Wang, S. A. Maloy, N. Mara, Nanohardness measurements of heavy ion irradiated coarse- and nanocrystalline-grained tungsten at room and high temperature, J. Nucl. Mater. 509 (2018) 276–284, https://doi.org/10.1016/j.jnucmat.2018.06.023.

[10] S. Das, H. Yu, E. Tarleton, F. Hofmann, Orientation-dependent indentation response of helium-implanted tungsten, Appl. Phys. Lett. 114 (2019), https://doi.org/10.1063/1.5097403.

[11] S. Das, H. Yu, K. Mizohata, E. Tarleton, F. Hofmann, Modified deformation behaviour of self-ion irradiated tungsten: a combined nano-indentation, HR-EBSD and crystal plasticity study, Int. J. Plast. 135 (2020), https://doi.org/10.1016/j.ijplas.2020.102817.

[12] S. Das, D.E.J. Armstrong, Y. Zayachuk, W. Liu, R. Xu, F. Hofmann, The effect of helium implantation on the deformation behaviour of tungsten: X-ray micro-diffraction and nanoindentation, Scr. Mater. 146 (2018) 335–339, https://doi.org/10.1016/j.scriptamat.2017.12.014.

[13] A. Seeger, Why anomalous slip in body-centred cubic metals? Mater. Sci. Eng. A 319–321 (2001) 254–260, https://doi.org/10.1016/S0921-5093(01)00958-3.

[14] B.D. Beake, S. Goel, Incipient plasticity in tungsten during nanoindentation: dependence on surface roughness, probe radius and crystal orientation, Int. J. Refract. Met. Hard Mater. 75 (2018) 63–69, https://doi.org/10.1016/j.ijrmhm.2018.03.020.

[15] H. Yu, S. Das, H. Yu, P. Karamched, E. Tarleton, F. Hofmann, Orientation dependence of the nano-indentation behaviour of pure tungsten, Scr. Mater. 189 (2020) 135–139, https://doi.org/10.1016/j.scriptamat.2020.08.014.

[16] T.P. Remington, C.J. Ruestes, E.M. Bringa, B.A. Remington, C.H. Lu, B. Kad, M. A. Meyers, Plastic deformation in nanoindentation of tantalum: a new mechanism for prismatic loop formation, Acta Mater. 78 (2014) 378–393, https://doi.org/10.1016/j.actamat.2014.06.058.

[17] Y.Z. Xia, H. Bei, Y.F. Gao, D. Catoor, E.P. George, Synthesis, characterization, and nanoindentation response of single crystal Fe-Cr-Ni alloys with FCC and BCC structures, Mater. Sci. Eng. A 611 (2014) 177–187, https://doi.org/10.1016/j.msea.2014.05.079.

[18] J. Alcalá, R. Dalmau, O. Franke, M. Biener, J. Biener, A. Hodge, Planar defect nucleation and annihilation mechanisms in nanocontact plasticity of metal surfaces, Phys. Rev. Lett. 109 (2012), https://doi.org/10.1103/PhysRevLett.109.075502.

[19] J. Varillas, J. Očenášek, J. Torner, J. Alcalá, Unraveling deformation mechanisms around FCC and BCC nanocontacts through slip trace and pileup topography analyses, Acta Mater. 125 (2017) 431–441, https://doi.org/10.1016/j.actamat.2016.11.067.

[20] D. Immel, M. Mrovec, R. Drautz, G. Sutmann, Nanoindentation simulations for copper and tungsten with adaptive-precision potentials, Phys. Rev. Mater. 9 (2025), https://doi.org/10.1103/2lkd-l6gt.

[21] Y. Sato, S. Shinzato, T. Ohmura, T. Hatano, S. Ogata, Unique universal scaling in nanoindentation pop-ins, Nat. Commun. 11 (2020), https://doi.org/10.1038/s41467-020-17918-7.

[22] F. Zhu, J. Tao, J. Wu, F. Zhou, J. Chen, Y. Pei, L. Song, J. Wu, D. Wang, Molecular dynamics simulation of the indentation behavior of tungsten with varying crystal orientations and Berkovich indenter orientations, Mater. Today Commun. 41 (2024), https://doi.org/10.1016/j.mtcomm.2024.110738.

[23] C.J. Ruestes, I.A. Alhafez, H.M. Urbassek, Atomistic studies of nanoindentation—a review of recent advances, Crystals (Basel). 7 (2017), https://doi.org/10.3390/cryst7100293.

[24] N.A. Stelmashenko, M.G. Walls, L.M. Brown, Y.V. Milman, Microindentations on W and Mo oriented single crystals: An STM study, Acta Metall. Mater. 41 (1993) 2855–2865, https://doi.org/10.1016/0956-7151(93)90100-7.

[25] Y. Zayachuk, D.E.J. Armstrong, K. Bystrov, S. Van Boxel, T. Morgan, S.G. Roberts, Nanoindentation study of the combined effects of crystallography, heat treatment and exposure to high-flux deuterium plasma in tungsten, J. Nucl. Mater. 486 (2017) 183–190, https://doi.org/10.1016/j.jnucmat.2017.01.026.

[26] B.D. Beake, A.J. Harris, J. Moghal, D.E.J. Armstrong, Temperature dependence of strain rate sensitivity, indentation size effects and pile-up in polycrystalline tungsten from 25 to 950 °C, Mater. Des. 156 (2018) 278–286, https://doi.org/10.1016/j.matdes.2018.06.063.

[27] X. Xiao, D. Terentyev, A. Ruiz, A. Zinovev, A. Bakaev, E.E. Zhurkin, High temperature nano-indentation of tungsten: modelling and experimental validation, Mater. Sci. Eng. A 743 (2019) 106–113, https://doi.org/10.1016/j.msea.2018.11.079.

[28] D. Terentyev, X. Xiao, S. Lemeshko, U. Hangen, E.E. Zhurkin, High temperature nanoindentation of tungsten: modelling and experimental validation, Int. J. Refract. Met. Hard Mater. 89 (2020), https://doi.org/10.1016/j.ijrmhm.2020.105222.

[29] K.L. Johnson, Contact mechanics, Cambridge University Press, 1985, https://doi.org/10.1017/CBO9781139171731.

[30] S. Zaefferer, N.N. Elhami, Theory and application of electron channelling contrast imaging under controlled diffraction conditions, Acta Mater. 75 (2014) 20–50, https://doi.org/10.1016/j.actamat.2014.04.018.

[31] F. Tropper, T. Ohmura, Direct observation of nanoindentation-induced punching-out of prismatic dislocation loops in tungsten [Article in preparation].

[32] A. Tripathi, S. Zaefferer, On the resolution of EBSD across atomic density and accelerating voltage with a particular focus on the light metal magnesium, Ultramicroscopy 207 (2019), https://doi.org/10.1016/j.ultramic.2019.112828.